ACS APPLIED ENERGY MATERIALS

www.acsaem.org
Article

Forensic and Performance Evaluation of Large Format Commercial Sodium-Ion Cells

Puritut Nakhanivej,* Maria J. Balart-Murria, Putthachat Sinted, Aohan Zhang, Tianxing Shi, Vincent A. Perry-French, Tanveerkhan S. Pathan, Julia Weaving, Rhodri Jervis, and Melanie J. Loveridge*

Cite This: ACS Appl. Energy Mater. 2026, 9, 5555−5563

ABSTRACT: Sodium-ion batteries (SIBs) are emerging as promising alternatives to lithium-ion batteries (LIBs) for automotive applications, highlighting the requirement of fundamental research to understand their components and functioning. In addition, large-format cylindrical cells are currently being explored for SIBs for use in electric vehicles. This study presents a safe and systematic methodology for the forensic analysis of large-format cylindrical SIB cells, focusing on how manufacturing influences their operational behavior and safety. Comprehensive evaluations of cell design and electrode and electrolyte chemistry were performed through advanced microscopic and spectroscopic characterization. Furthermore, three-electrode cells were reconstructed from harvested electrodes to more deeply assess electrochemical performance, including cycle life, efficiency, and rate capability. This reverse-engineering approach establishes a robust foundation for evaluating SIB performance metrics and enables a direct comparison with commercial LIBs. The findings are essential for optimizing SIB design and guiding selection of the most suitable battery chemistry for specific end-user applications.

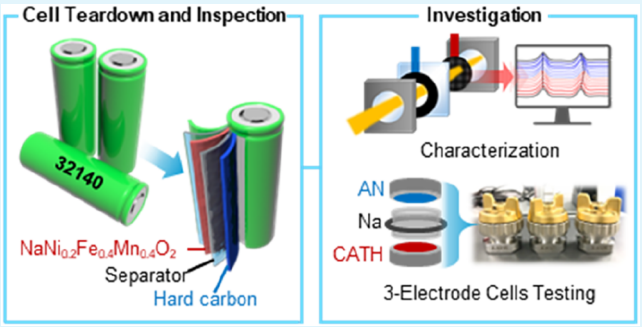

KEYWORDS: *sodium-ion batteries, cylindrical cells, O3-type nickel iron manganese oxide, reverse engineering, battery forensics*

1. INTRODUCTION

The rapid growth in demand for electric vehicles (EVs) and micromobility solutions has driven the need for scalable, cost-effective, and sustainable energy-storage technologies. While lithium-ion batteries (LIBs) currently dominate the market, concerns over the long-term availability of lithium resources and associated supply chain vulnerabilities have raised questions about their sustainability for widespread electrification.[1] In particular, the predicted lithium shortage poses a significant bottleneck for future battery production.[2−4]

Sodium-ion batteries (SIBs) have recently emerged as a promising alternative to LIBs due to their reliance on more abundant and geopolitically secure raw materials.[5,6] Moreover, SIB chemistries can be designed without cobalt, further improving their environmental, geopolitical, and ethical footprint.[7−9] Reflecting this shift in interest, several major LIB manufacturers have announced plans to expand their production capabilities to include sodium-ion technologies.[10] To meet the energy demands of EV and micromobility applications, SIBs must achieve higher specific energy at the cell level, which often necessitates the use of larger cell formats beyond conventional 18650 or 21700 cylindrical cells. Although initial demonstrations toward SIB commercialization have utilized cathode materials such as layered transition metal oxides,[11] (fluoro)-phosphates,[12−15] and Prussian blue analogues,[16−18] these materials typically exhibit low capacities, limiting the overall energy density of the cells.[19] In addition, scaling to larger cell formats introduces increased concerns regarding the safety and cost. Therefore, advancements in electrolyte formulation aimed at enhancing the intrinsic safety of SIBs[20] and strategies to mitigate metal ion plating,[21] as well as improvements in electrode processing methodologies to enable scalable and cost-effective manufacturing[22] must be carefully considered alongside materials development.

These concerns and limitations underscore the urgent need for more comprehensive data on commercial SIBs—especially large-format cells—to better understand the interplay between cell design and electrochemical performance.[23−27] In this work, we present a safe and systematic reverse engineering approach for large-format (32140) commercial SIBs. Our methodology includes detailed characterization of electrodes using microscopic and spectroscopic techniques, analysis of electrolytes via multinuclear magnetic resonance (NMR) spectroscopy, and

Received: December 16, 2025
Revised: April 13, 2026
Accepted: April 14, 2026
Published: April 24, 2026

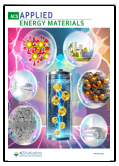

reconstruction of three-electrode (3E) cells to evaluate electrochemical behavior, including cycling and rate performance. The insights gained from this study contribute to a deeper understanding of the design principles that govern performance in large-format SIBs and offer valuable feedback for the development of next-generation sodium-ion technologies.

2. EXPERIMENTAL SECTION

2.1. Cell Disassembly

The cells were fully discharged to 0% SOC prior to transferring to an Ar-filled MBraun glovebox, which always maintained the moisture and oxygen levels below 0.1 ppm. The following steps were followed to open the cell (see Figures S1 and S2): The as-received cell was weighed. The top protective plastic film was removed, and the cell was weighed again. The cover plastic was removed, and the top cap was cut open with a pipe cutter. The cathode current collector tab was detached from the top cap, and the top cap and the cell body were weighed separately. The steel can was removed gently, and the can body and jelly roll were weighed separately. The jelly roll was opened for a visual inspection of electrodes and separators. Each internal component was weighed separately. All of the components were stored inside the glovebox for 24 h and then weighed again to account for electrolyte mass.

2.2. Characterization

Cross sections for the scanning electron microscope (SEM) were prepared by Ar broad-beam ion milling (BBIM). Pieces of the anode and cathode were prepared in an Ar Glovebox and transferred to a Hitachi IM4000Plus ion milling system equipped with an air protection unit. Cross-section milling was performed at 6 kV for 2.5 h with 40° stage rocking. The samples were then transferred back to a glovebox using the IM4000Plus air protection capsule. The cross sections were then transferred to a Thermo Scientific Scios Dualbeam using the CleanConnect inert gas transfer system for imaging without exposure to air. The SEM images were acquired using accelerating voltage 2.0 kV and beam current 0.1 nA. Energy dispersive X-ray spectroscopy (EDS) mappings were acquired using Oxford Instruments UltiMax 170.

X-ray diffraction (XRD) measurements of the anode and cathode were performed using a Panalytical Empyrean with a Mo target and solid-state PiXcel detector. The Rietveld refinement of the cathode was done using TOPAS software with the parameters shown in Table S1.

X-ray fluorescence (XRF) experiments were carried out, using a Rigaku Primus IV wavelength dispersive XRF spectrometer (WDXRF) equipped with a 4 kW Kα rhodium X-ray source. Samples were analyzed as solids, using an "EZ Scan" protocol which performs an element sweep from B−U. With the use of a LiF (200) crystal analyzer to measure Kα emissions in the 4300 to 1200 eV energy range, the fluorescent signal for the emission lines of the 3d transition metals (TM) of interest (Mn, Ni, Fe, and Cu) was optimized to measure TM deposition on cathode samples. Cathode sample squares of 2 cm × 2 cm were obtained after the cell disassembling process and mounted in air in samples holders with a 20 mm diameter mask. The mounting process was carried out in air since we were more interested on the TM presence rather than the chemical specification.

The X-ray photoelectron spectroscopy (XPS) data were collected at the Photoemission Research Technology Platform, University of Warwick. The samples investigated in this study were prepared in an mBRAUN LabMaster Pro argon glovebox using electrically conductive carbon tape, mounted on to a Cu sample stub with a layer of filter paper between the samples and the sample bar to ensure electrical isolation and hence mitigate differential charging. The samples were then transferred in an inert transfer vessel to a Kratos Axis Ultra DLD spectrometer which possesses a base pressure below 1×10^{-10} mbar. XPS measurements were performed in the main analysis chamber, with the sample being illuminated using a monochromated Al Kα X-ray source (hν = 1486.7 eV). The measurements were conducted at room temperature and at a takeoff angle of 90° with respect to the surface parallel. The core level spectra were recorded using a pass energy of 20 eV (resolution approximately 0.4 eV), from an analysis area of 300 μm × 700 μm. The work function and binding energy scale of the spectrometer were calibrated using the Fermi edge and $3d_{5/2}$ peak recorded from a polycrystalline Ag sample prior to the commencement of the experiments. To prevent surface charging, the surface was flooded with a beam of low energy electrons from a charge neutralizer throughout the experiment, and this necessitated recalibration of the binding energy scale. To achieve this, the C−C/C−H component in the C 1s spectrum was referenced to 285.0 eV. The data were analyzed in the CasaXPS package using Shirley backgrounds and mixed Gaussian−Lorentzian (Voigt) lineshapes, with asymmetry parameters where appropriate.

X-ray computed tomography (XCT) of the top cap was scanned using a Metrotom 1500 (Carl Zeiss GmbH). The voxel size was 56.3 μm. The tube settings were fixed at a voltage of 220 kV and a power of 48 W, with a 0.75 mm Cu filter in place. For scanning, a total of 3000 projections were acquired at a source-to-detector distance (SDD) of 1450 mm. To improve image quality, each projection employed an effective 1 s exposure time, achieved by averaging four individual frames, each exposed for 0.25 s. The raw XCT data were managed and reconstructed using the Metrotom OS 3, with subsequent analysis, visualization, and measurement of the volumetric data performed in VG Studio Max 2024.1.

Nuclear magnetic resonance (NMR) spectroscopy of the liquid electrolyte sample was conducted using a nuclear NMR Bruker Avance III HD 400 MHz, focusing on ^{1}H, ^{19}F, and ^{31}P nuclei. The bulk free electrolyte remaining in the casing was collected (see Figure S2b) and diluted in a 1:10 v/v ratio with chloroform-d (Merck). The solvent contained 0.03 vol % tetramethylsilane (TMS) as an internal standard, with a minimum deuteration degree of 99.8% (stabilized with silver). The diluted solution sample was filtered using SPARTAN regenerated cellulose syringe filters (diameter of 30 mm and pore size of 0.45 μm) and subsequently transferred to Wilmad NMR tubes with a 5 mm diameter.

Simultaneous thermal analysis (STA) was conducted using a PerkinElmer STA 8000 over a temperature range of 50−600 °C at a heating rate of 15 °C min^{-1}. The sample mass was 33.13 mg. A stainless-steel calibration ball with a mass of 28.05 mg was used for calibration.

2.3. Three-Electrode Cell Fabrication

To prepare electrode discs for 3E-cell fabrication, the electrodes from the jelly roll needed to be cut, rinsed, and have one side of the coating removed. These activities were performed in the same Ar-filled glovebox used for the teardown process. The following procedure was followed to harvest and fabricate 3E cells: After disassembling the cell and unrolling the jelly roll, both electrodes (anode and cathode) were cut at the middle of the jelly roll to the desired width (approximately 13 cm) and rinsed with dimethyl carbonate (DMC, ≥99% anhydrous, Merck). The rinsed electrodes were left for 30 min to allow the residual DMC to evaporate. Then, the electrodes were attached to flat acrylic plates using Kapton tape as shown in Figure S8 (masking the edges to prevent NMP from seeping into the coating on the other side). One side of the electrode coating was removed by gently rubbing using a soft sponge with 1-methyl-2-pyrrolidinone (NMP, 99.5% anhydrous, Merck). Then, one-sided electrode sheets were cut into circular discs using EL-cell cutters (18 mm diameter). The anode and cathode discs were transferred to separate Buchi tubes. Then, the Buchi tubes were moved out of the glovebox and placed in Buchi glass ovens (Buchi B-585) for drying. The anode discs were dried under dynamic vacuum at 120 °C for 12 h, while the cathode discs were dried with two different conditions: at 120 °C for 12 h and at 180 °C for 12 h. Subsequently, the 3E cells were assembled inside the glovebox using ECC-PAT-core component (EL-CELL). The prepared cathode and anode discs served as working and counter electrodes, respectively. The insulation sleeve with an in-built Na ring served as the reference electrode. The insulation sleeve had an in-built Whatman Borosilicate glass fiber separator of 260 μm thickness. The electrolyte was 150 μL of 1 M $NaPF_6$ in EC/DEC (3/7 v/v%) + 2 wt % FEC. The 3E cells without the FEC additive were also made to study the effect of additive. The 3E cells were tested using a potentiostat cycler (Biologic VMP3) with a constant current−constant voltage (CCCV) method in a 25 °C temperature-

https://doi.org/10.1021/acsaem.5c03924
ACS Appl. Energy Mater. 2026, 9, 5555−5563

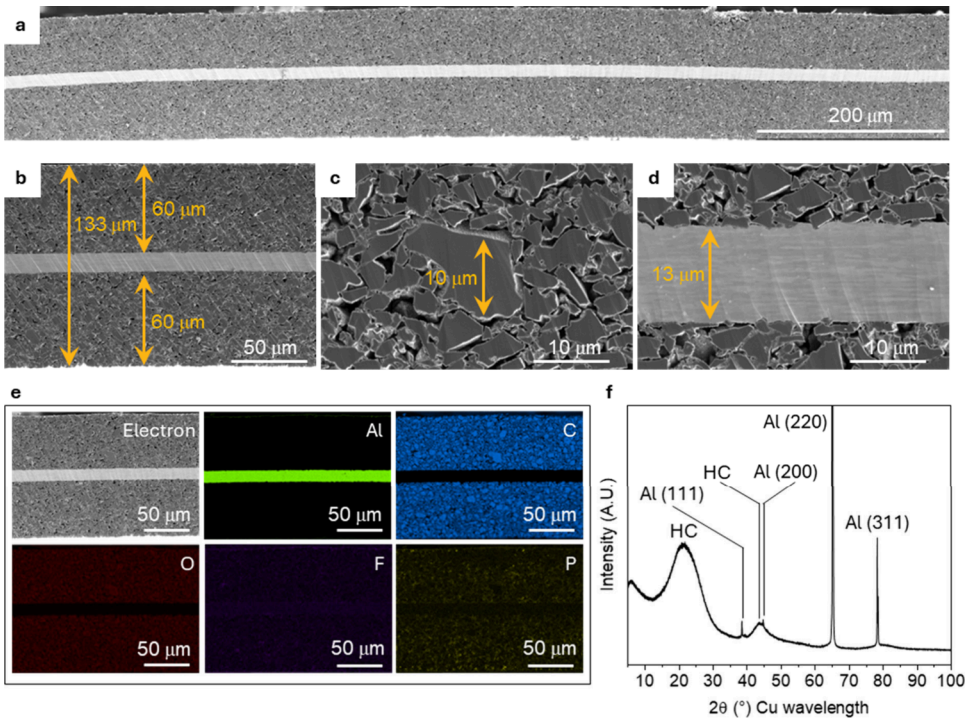

Figure 1. Characterization of anode. (a–d) Cross-section SEM images. (e) EDS elemental mapping. (f) XRD pattern where HC stands for hard carbon.

controlled oven. The formation cycles were performed at a C/20 rate for two cycles, with a voltage limit of 1.5–3.9 V. The charge/discharge rate tests were run at C/10, C/5, C/3, 1C, 2C, and 3C, while the long cycle tests were run at C/3 within this voltage limit. Charge and discharge rates were the same.

3. RESULTS AND DISCUSSION

3.1. Cell Design

The cells studied in this work comprise a steel can and top cap with a groove or neck between them, which allowed for the placement of a pipe cutter blade for opening. The jelly roll is designed without tabs,[28] as illustrated in Figures S1 and S2 in the Supporting Information. An excess amount of electrolyte was observed, which was extracted for further compositional analysis using NMR spectroscopy. XCT scans of the top cap revealed a design similar to commercial Li-ion cylindrical cells[29] (Figure S3 in the Supporting Information). Specifically, there were venting and bottom disks, separated by a plastic disk, integrated into the upper outer jacket (upper part of the cell housing). No electronic protection components for overcharging were observed in the top cap during XCT scanning.

3.2. Morphology and Chemistry of Anode and Cathode

In order to evaluate the coating morphology and thickness, SEM images were acquired through a cross-sectional view, using a broad-beam ion miller to cut the cross sections. The cross-sectional SEM images and EDS elemental mapping of the anode are presented in Figure 1a–e. As shown in Figure 1a, the anode features a double-sided coating that remained intact after dismantling the cell. Since this was a fresh electrode, having only undergone formation cycles, no cracks or mechanical damage were observed. The particle morphology in Figure 1b–d suggests that the anode material is hard carbon (which is further verified through XRD in a later section), with particle sizes below 10 μm. The coating thickness was measured at 60

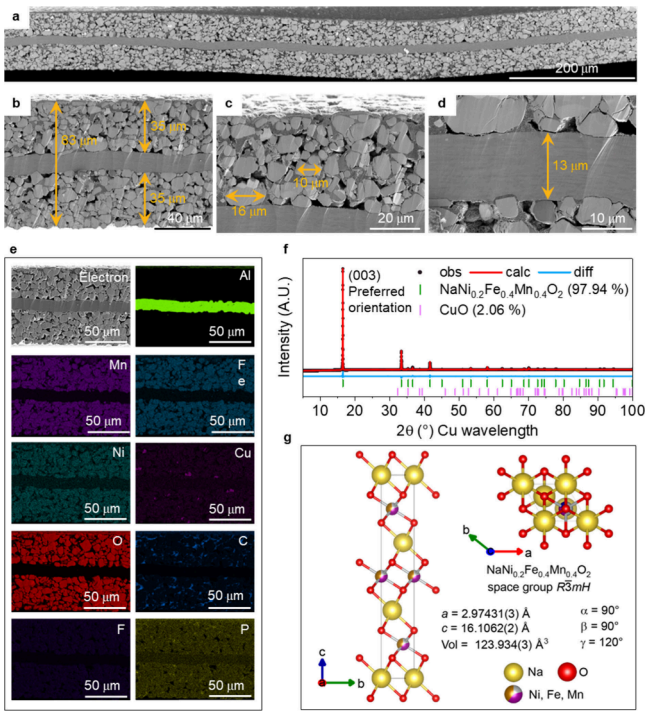

Figure 2. Characterization of cathode. (a–d) Cross-section SEM images. (e) EDS elemental mappings. (f) XRD pattern with Rietveld refinement result and diffraction patterns of standard $NaNi_{0.2}Fe_{0.4}Mn_{0.4}O_2$ and CuO. (g) Crystal structure derived from Rietveld refinement in (f). The numbers in brackets indicate the error from calculation, e.g., 2.97431(3) means 2.97431 ± 0.00003.

μm on each side, with an Al foil current collector measuring 13 μm in thickness. It is worth noting that Al foil is commonly used as the current collector for anodes in sodium-ion batteries

https://doi.org/10.1021/acsaem.5c03924
ACS Appl. Energy Mater. 2026, 9, 5555–5563

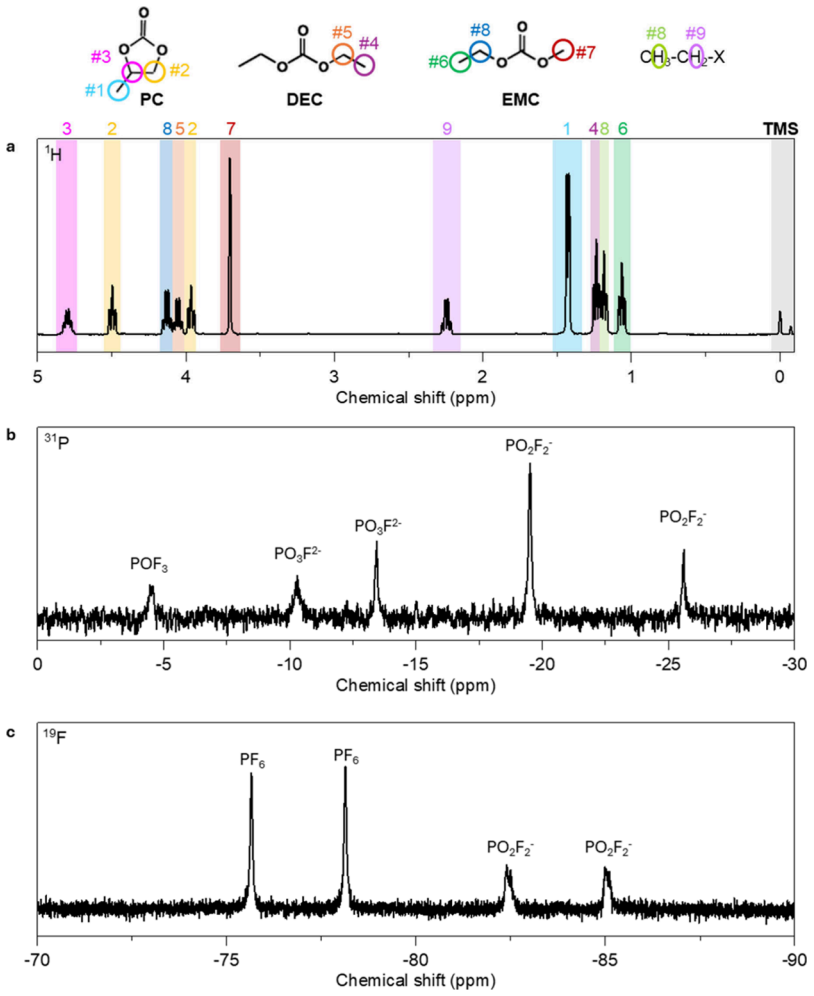

Figure 3. Characterization of electrolyte. ^{1}H (a), ^{31}P (b), and ^{19}F (c) NMR spectra of electrolyte extracted from cylindrical cell.

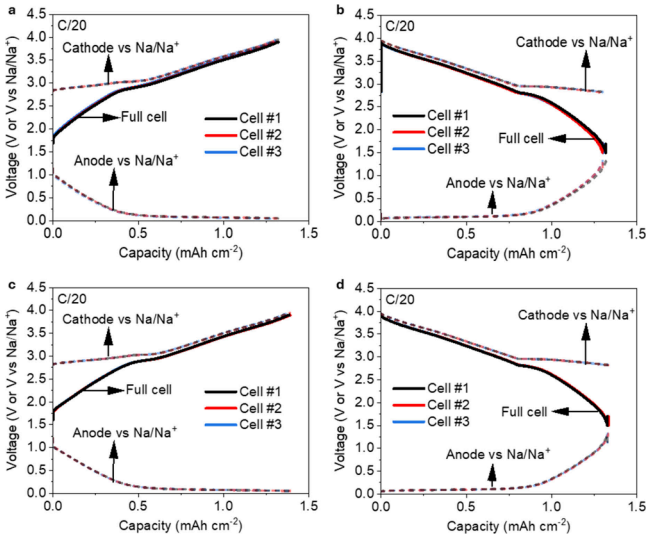

Figure 4. Formation cycle of 3E cells. (a–d) Charge/discharge profiles of 3E cells at C/20 using electrodes harvested from cylindrical cell with drying temperatures of cathode of 180 °C (a, b) and 120 °C (c, d).

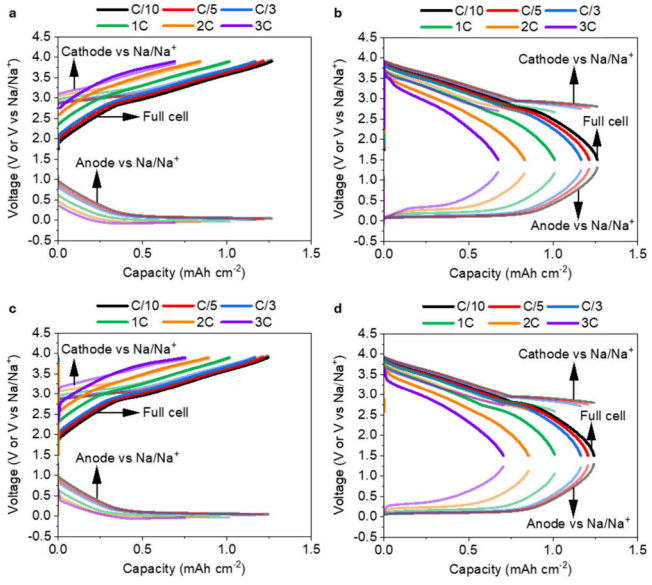

Figure 5. Rate test of 3E cells. (a–d) Charge/discharge profiles of 3E cells at different C rates using electrodes harvested from cylindrical cell with drying temperature of cathode of 180 °C (a, b) and 120 °C (c, d).

(SIBs) since Al is cost effective and does not alloy with Na at low potentials in contrast to the case with Li.[11] The volume fractions of the active material, carbon-binder domain, and pores were 62%, 14%, and 24%, respectively, estimated by processing grayscale contrast of these three elements in 2D cross-sectional SEM image. It should be noted that this is to provide the idea of

https://doi.org/10.1021/acsaem.5c03924
ACS Appl. Energy Mater. 2026, 9, 5555−5563

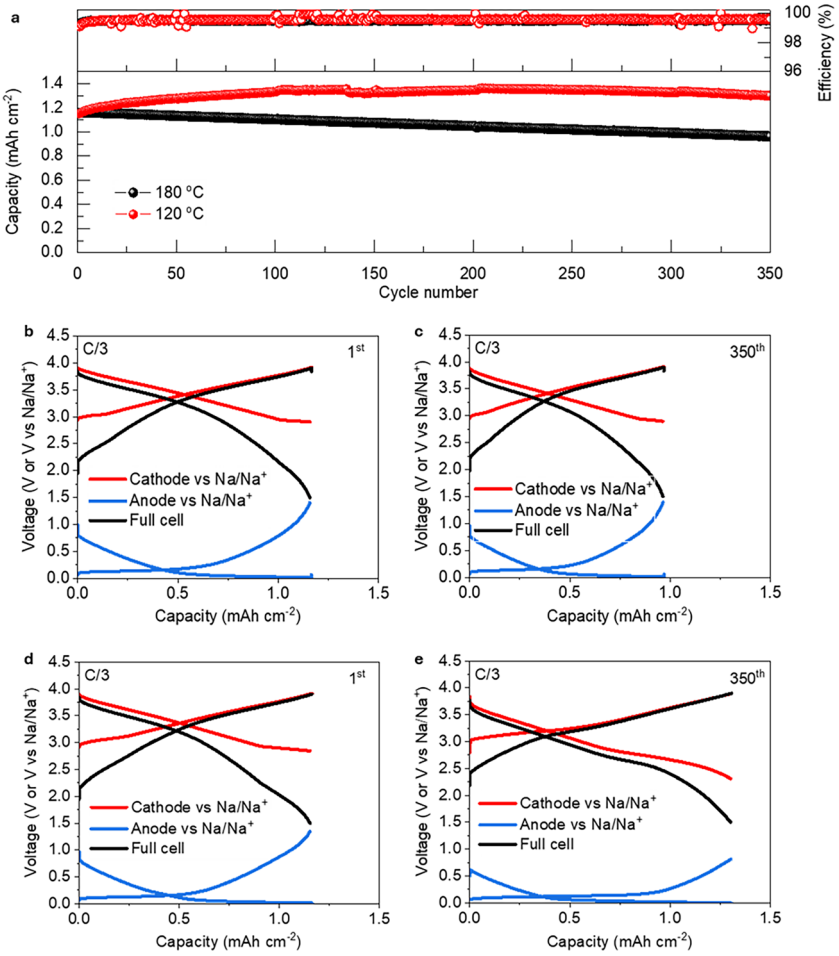

Figure 6. Cycle test of 3E cells. (a) Cycle stability of 3E cells cycled at C/3. (b–e) Charge/discharge profiles of 3E cells at first and 350th cycle using electrodes harvested from cylindrical cell with drying temperatures of cathode of 180 °C (b, c) and 120 °C (d, e).

volume fraction, and the assumption should be taken that the coating is isotropic where the 2D area fraction ≈ 3D volume fraction (Delesse principle). The true 3D connectivity could be achieved from a 3D plasma-focused-ion-beam SEM image, but this was not performed in this work. Elemental mapping in Figure 1e confirms the presence of Al in the current collector foil. Additionally, carbon and oxygen were uniformly distributed throughout the coating, confirming the use of pure hard carbon as the active anode material. Minor signals of F and P are likely attributable to polyvinylidene fluoride (PVDF) binder and residual electrolyte components, such as sodium salt and solvents. XRD patterns of the anode are shown in Figure 1f. The diffraction peaks from the Al foil are observed at $2\theta = 38°$, 45°, 65°, and 79°. Two distinct peaks appear at $2\theta = 23°$ and 43°, confirming the diffraction planes of hard carbon.

Figure 2a–e presents the cross-sectional SEM images and EDS elemental mapping of the cathode. Similar to the anode, the cathode featured a double-sided coating that remained intact following the full disassembly process (Figure 2a). As shown in Figure 2b–d, the coating thickness was approximately 35 μm on each side, while the Al foil current collector measured 13 μm in thickness. The cathode material was composed of single crystal particles with sizes ranging from 5 to 16 μm. The volume fractions of active material, carbon-binder domain, and pores were 68%, 11%, and 21%, respectively. Elemental mapping in Figure 2e suggests that the cathode material consists of a mixed metal oxide compound containing Ni, Fe, and Mn, indicating that the general composition of the active material is $Na_xNi_yFe_zMn_{1-y-z}O_2$ (NFM). In addition, a weak Cu signal was detected, indicating probable Cu doping from the manufacturer, resulting in slight Cu dispersion within mixed metal oxide and several CuO_x particles formed. Based on the EDS spectra (averaged from 34 scans), the composition is $Na(Ni_{0.26}Fe_{0.36}Mn_{0.38})O_2$. The C, F, and P signals detected are attributed to the binder and residues from the electrolyte ($NaPF_6$ salt and solvents). The XRD pattern of the cathode in Figure 2f shows several sharp diffraction peaks, indicating the high degree of crystallinity of the active material. Rietveld refinement identified the cathode composition as $Na(Ni_{0.2}Fe_{0.4}Mn_{0.4})O_2$, an O3-type layered compound with a hexagonal crystal system and belonging to the $R\bar{3}m$ space group as shown in the crystal structure in Figure 2g (see Table S1 in Supporting Information for Rietveld refinement parameters). In addition, the refinement suggests that the cathode is composed of 97.94% $Na(Ni_{0.2}Fe_{0.4}Mn_{0.4})O_2$ and 2.06% CuO (crystal structure shown in Figure S4 in Supporting Information), due to the Cu doping. Studies have shown that a facile copper doping process enhances the surface structural stability of Mn-rich layered oxide cathodes in Na-ion batteries.[30] Cu doping has also been reported to mitigate the Jahn–Teller effect, augment the electrical conductivity of the material, and diminish charge transfer resistance.[31] The volume fraction and chemical composition of the active materials were used to estimate the negative-to-positive capacity (N/P) ratio. Both cathode and

https://doi.org/10.1021/acsaem.5c03924
ACS Appl. Energy Mater. 2026, 9, 5555–5563

anode electrodes were punched into 10 cm^2 discs, and the average coating mass was measured after subtracting the current collector foil weight. The active material mass for each electrode was then calculated based on the active material volume fraction. Assuming practical specific capacities of 140 mAh g^{-1} for Cu-doped $Na(Ni_{0.2}Fe_{0.4}Mn_{0.4})O_2$[32] and 270 mAh g^{-1} for hard carbon,[33] the estimated N/P capacity ratio is 1.16. Detailed calculations are provided in section S4 and Figure S5 of the Supporting Information.

To further confirm the cathode composition, XRF measurements were conducted. The bar plot in Figure S6 displays the atomic fractions of the detected elements. Based on the relative atomic fractions of Ni, Fe, and Mn, the cathode composition was determined to be approximately $Na(Ni_{0.24}Fe_{0.39}Mn_{0.37})O_2$, which is in agreement with the results obtained from XRD and EDS analyses. Additionally, the weight fraction data indicated a Cu content of 3.7 wt %, attributed to Cu doping, presenting as Cu in a mixed metal oxide and CuO_x particles, as previously observed in the elemental mapping (Figure 2e). The XPS analysis was also performed to complement the results (see section S6 and Figure S7 in Supporting Information). However, owing to the surface-sensitive nature of the technique (~5 nm), it is unable to detect TMs located deeper within the bulk cathode material, with only $NaPF_6$ salt being detected.

3.3. Analysis of Electrolyte

The residual free electrolyte remaining in the cell casing was collected and diluted with NMR-grade chloroform at a ratio of 1:10 v/v. A 0.5 mL of this solution was then transferred to a standard NMR tube for analysis, focusing on ^1H, ^{17}F, and ^{31}P nuclei (Figure 3). The ^1H NMR spectrum indicated that the solvents in the electrolyte were PC/DEC/EMC (5:2:3 wt), as detailed in Table S2 in the Supporting Information for semiquantitative analysis. It is our assessment that this cell has undergone formation; after the formation cycle, the $NaPF_6$ salt and PC/DEC/EMC solvents partially decompose, resulting in the formation of POF_3, $PO_3F_2^-$, and $PO_2F_2^-$ anions, as evidenced by the ^{31}P and ^{19}F spectra. There were no byproducts from $NaPF_6$ degradation into HF, confirming the relatively fresh condition of this cell. The presence of the combination between linear carbonate solvents, DEC and EMC, is likely to be for enhanced wettability.[34] This is because PC solvent alone is unable to penetrate hydrophobic polyethylene/polypropylene (PE/PP)-based separators. The partially positively charged ethyl groups (CH_3CH_2) in EMC and DEC are compatible with hydrophobic separators, while their carbonate moieties ($-OCO_2-$) tend to interact with polar PC, thus improving wettability.[35] In addition, it has been reported that fluoroethylene carbonate (FEC) can act as an electrolyte additive, serving as an effective SEI- and CEI-forming agent to enhance cell lifetime.[36] However, if FEC had been present in the electrolyte, it may have been substantially consumed during the formation cycle. Therefore, it cannot be definitively confirmed whether the electrolyte originally contained FEC, as the cells were received postformation. Indirect evidence is provided by our XPS analysis, which indicates the presence of Na_2CO_3 and $ROCO_2Na$ species in the CEI. These decomposition products are commonly associated with the breakdown of FEC additives[37] (see Supporting Information S6). Nevertheless, it should be clearly acknowledged that the identification of an electrolyte additive is intrinsically limited by the postformation condition in which the cells were received.

3.4. Electrochemical Performance Evaluation

3E cells (parallel testing model, PAT) were fabricated using electrodes harvested from the cylindrical cell (see Figure S8 in Supporting Information for the electrode harvesting process). The integrity of the harvested electrodes was validated through comparison of the voltage profiles of the 3E cell and the original cylindrical cell (see Supporting Information S9). It is also worth noting that the N/P ratio in reconstructed 3E cells may deviate from that of the original cell, particularly for certain cell chemistries and formats. Therefore, incorporating an appropriate anode overhang area should be considered in future methodological developments to better control the N/P ratio and ensure a closer replication of the original cell configuration.

Since NFM is very sensitive to moisture and oxygen, we employed two different drying temperatures to the harvested cathode (120 and 180 °C) to optimize the drying process. Figure 4 shows the reformation cycles of 3E cells with cathode drying temperature of 120 and 180 °C.[38] It can be clearly seen that both sets of cells have the same electrochemical behavior at C/20 regardless of the drying temperatures of the cathode. The discharge capacity of both sets of 3E cells was 1.33 mAh cm^{-2}. This is probably due to two cycles of the slow C rate applied; however, we expect to see an electrochemical performance difference when employing a running cycle at a higher C rate. The anode profiles indicate the typical Na-ion (de)insertion into interlayer of hard carbon (i.e., slope profiles above 0.2 V vs Na/Na^+ and low voltage plateau below 0.2 V vs Na/Na^+).[39] For the cathode profile, the charge/discharge curves can be divided into two sections: a long plateau around 2.8−3.0 V vs Na/Na^+ and a sloping part above 3.0 V vs Na/Na^+. The voltage plateau is attributed to the phase transformation from O3 to P3 phases while the sloping line at higher voltage is due to a solid-solution reaction with the P3 structure.[40] This charge storage mechanism has been verified by in situ XRD from previous literature by Yao et al.[41]

The rate capabilities of 3E cells with cathode drying temperatures of 120 and 180 °C are shown in Figure 5. Using 3E cells allow us to simultaneously observe the rate performance and electrochemical behavior of cathode, anode, and full cell. Both sets of cells exhibited similar discharged capacity of 1.24, 1.20, 1.16, 1.00, 0.85, and 0.70 mAh cm^{-2} at C rates of C/10, C/5, C/3, 1C, 2C, and 3C, respectively, giving 56% of its capacity when comparing 3C with C/10. The TM (such as Fe and Cu) substitution can facilitate the Na-ion kinetics.[42,43] The substitution of such TMs could suppress various phase transformations of typical layered $NaNi_{0.5}Mn_{0.5}O_2$ (i.e., $O3_{hex.} - O3'_{mon.} - P3_{hex.} - P3'_{mon.} - P3''_{hex.}$) materials above 3.0 V. It also extends the solid solution zone with the P3 phase (a sloping part above 3.0 V) and enlarges the interlayer distance, thereby improving structural stability and rapid Na^+ diffusion.[44] At higher C rates (2C and 3C), the plateau region of the cathode profile around 2.8−3.0 V vs Na/Na^+ was very minor, and the slope profile becomes more prominent, suggesting the solid solution dominates the Na-ion storage. This mechanism provides advantages for high-power applications. However, further developments are still required for this particular cell chemistry since the capacity drops significantly at higher C rates.

Since it was suspected that the binder of this cathode could be PVDF, which could be degraded during the drying process and affect the long-term cycling performance, we performed long-term cycling at C/3 for 3E cells comparing cathode drying temperatures of 120 and 180 °C as presented in Figure 6. The stability of the sodium reference electrode potential was

https://doi.org/10.1021/acsaem.5c03924
ACS Appl. Energy Mater. 2026, 9, 5555−5563

validated by monitoring the open circuit voltage of the cathode and anode vs Na/Na^+ after 100 cycles (see Supporting Information S10). After 350 cycles, the cells with a 180 °C cathode drying temperature showed 83% capacity retention, while the capacity of cells with 120 °C achieved higher capacity compared to the first cycle (112%). The over 100% capacity retention is explained by the fact that we have added fresh electrolyte after the electrodes were already formed. This procedure increased the available Na-ion inventory, allowing the capacity to rise during the initial cycles as the electrolyte gradually permeated the electrode pores and improved wetting. In contrast, this behavior was not observed in cells dried at 180 °C. At this temperature, the PVDF binder was softened and damaged during drying, as later confirmed by simultaneous thermal analysis (STA) performed on a harvested cathode sample (as described in the Characterization section and shown in Figure S11 of the Supporting Information). The degradation of PVDF led to pore collapse and deterioration of the coating integrity.[45] The STA result of the cathode sample indicates that PVDF begins to melt at approximately 170 °C, while no thermal degradation of $NaNi_{0.2}Fe_{0.4}Mn_{0.4}O_2$ was detected at this temperature (see Supporting Information S11 for the corresponding mass loss and heat flow profiles). In particular, the 3E profiles at the 350th cycle suggested that the cells with 180 °C were dominated by solid solution behavior only, exhibiting lower capacity. Conversely, the cell with 120 °C still exhibited both solid solution and O3−P3 phase transformation, hence achieving higher capacity.

4. CONCLUSION

As confirmed through various characterization techniques, the large format commercial Na-ion cells feature a cathode composed of $NaNi_{0.2}Fe_{0.4}Mn_{0.4}O_2$ with 3.7 wt % Cu/CuO_x distribution and a hard carbon anode. The electrolyte used in these cells was $NaPF_6$ in PC/DEC/EMC (5:2:3 by weight). The cells employ a tabless cylindrical design with 32140 dimensions. Electrochemical reverse engineering identified the charge storage mechanism of the $NaNi_{0.2}Fe_{0.4}Mn_{0.4}O_2$ (with 3.7 wt % Cu/CuO_x distribution) as being governed by two key processes: O3−P3 phase transformation (occurring between 2.8−3.0 V vs Na/Na^+) and solid solution behavior (above 3.0 V vs Na/Na^+). The solid solution reaction was originated by the Fe and Cu substitution which enhances the kinetic diffusion of Na ion. This mechanism becomes particularly dominant at high C rates, as evidenced by the voltage profiles of 3E cells at 2C and 3C, demonstrating the material's capability for high-power applications.

Reverse engineering case studies such as this—based on disassembly, multiple length-scale metrology and electrochemistry—are valuable for advancing battery technology. They enable a deeper understanding of the functionality and design of each component because the interplay between cell format and architecture dictates overall cell behavior. Such studies are instrumental in leading to improvements in chemistry, electrode microstructures, additives, and the composition of the many interfaces that govern battery stability and safety. Moreover, this work highlights the scientific value of open data, as the findings can support battery modeling and further research. It can also help forecast research directions aligned with commercial developments, especially since much academic focus currently lies on polyanionic compounds, Prussian blue analogues, and fluorophosphates rather than layered mixed metal oxides.[46,47]

■ ASSOCIATED CONTENT

Supporting Information

The Supporting Information is available free of charge at https://pubs.acs.org/doi/10.1021/acsaem.5c03924.

Supplementary experimental methods, cell teardown and inspection, XCT scans of top cap, crystal structure of CuO, calculation of negative−positive capacity (N/P) ratio, XRF data of cathode, XPS data of cathode, semiquantitative analysis of electrolyte, electrode harvesting for 3E cell reconstruction, effect of electrode harvesting process, stability of sodium reference electrode potential in 3E cells, and thermal analysis of cathode (PDF)

■ AUTHOR INFORMATION

Corresponding Authors

Puritut Nakhanivej − *WMG, University of Warwick, Coventry CV4 7AL, United Kingdom; The Faraday Institution, Quad One, Harwell Science and Innovation Campus, Didcot OX11 0RA, United Kingdom;* orcid.org/0000-0003-4052-9534; Email: Puritut.Nakhanivej@warwick.ac.uk

Melanie J. Loveridge − *WMG, University of Warwick, Coventry CV4 7AL, United Kingdom; The Faraday Institution, Quad One, Harwell Science and Innovation Campus, Didcot OX11 0RA, United Kingdom;* orcid.org/0000-0003-2908-3885; Email: M.Loveridge@warwick.ac.uk

Authors

Maria J. Balart-Murria − *WMG, University of Warwick, Coventry CV4 7AL, United Kingdom; The Faraday Institution, Quad One, Harwell Science and Innovation Campus, Didcot OX11 0RA, United Kingdom*

Putthachat Sinted − *Department of Chemistry, University of Warwick, Coventry CV4 7AL, United Kingdom;* orcid.org/0000-0002-2769-8731

Aohan Zhang − *Department of Physics, University of Cambridge, Cambridge CB3 9DF, United Kingdom; The Faraday Institution, Quad One, Harwell Science and Innovation Campus, Didcot OX11 0RA, United Kingdom*

Tianxing Shi − *The Queen's College, University of Oxford, Oxford OX1 4AW, United Kingdom; The Faraday Institution, Quad One, Harwell Science and Innovation Campus, Didcot OX11 0RA, United Kingdom;* orcid.org/0009-0002-8891-1572

Vincent A. Perry-French − *WMG, University of Warwick, Coventry CV4 7AL, United Kingdom*

Tanveerkhan S. Pathan − *WMG, University of Warwick, Coventry CV4 7AL, United Kingdom;* orcid.org/0000-0003-4192-5109

Julia Weaving − *Department of Chemical Engineering, University College London, London WC1E 7JE, United Kingdom; The Faraday Institution, Quad One, Harwell Science and Innovation Campus, Didcot OX11 0RA, United Kingdom*

Rhodri Jervis − *Department of Chemical Engineering, University College London, London WC1E 7JE, United Kingdom; Advanced Propulsion Lab, Marshgate, University College London, London E20 2AE, United Kingdom; The Faraday Institution, Quad One, Harwell Science and*

https://doi.org/10.1021/acsaem.5c03924
ACS Appl. Energy Mater. 2026, 9, 5555−5563

Innovation Campus, Didcot OX11 0RA, United Kingdom;
orcid.org/0000-0003-2784-7802

Complete contact information is available at:
https://pubs.acs.org/10.1021/acsaem.5c03924

Author Contributions

Puritut Nakhanivej: Writing – original draft, Methodology, Data curation, Formal analysis, Investigation, Visualization, Conceptualisation. **Maria J. Balart-Murria:** Methodology, Data curation, Formal analysis. **Putthachat Sinted:** Methodology, Data curation, Formal analysis. **Aohan Zhang:** Methodology, Data curation, Formal analysis. **Tianxing Shi:** Writing – original draft, Data curation, Formal analysis. **Vincent A. Perry-French:** Methodology, Data curation, Formal analysis. **Tanveerkhan S. Pathan:** Methodology, Data curation, Formal analysis, Validation. **Julia Weaving:** Funding acquisition, Project administration. **Rhodri Jervis:** Writing – review and editing, Funding acquisition, Project administration. **Melanie J. Loveridge:** Writing – review and editing, Funding acquisition, Project administration, Validation, Conceptualization. The manuscript was written through contributions of all authors. All authors have given approval to the final version of the manuscript.

Notes

The authors declare no competing financial interest.

■ ACKNOWLEDGMENTS

This work was kindly supported by the Faraday Institution SafeBatt project (Grant numbers FIRG061 and FIRG086). XCT data used in this article were acquired at the National Facility for X-ray Computed Tomography (NXCT) and carried out at the Centre for Imaging, Metrology, and Additive Technologies (CiMAT) at the University of Warwick under EPSRC Project Number EP/T02593X/1, the authors thank Dr. Evelien Zwanenburg for the technical support and scientific inputs. The authors are grateful to Dr. Ivana Hasa, Dr. Faduma Maddar, and Carla Albenga for the resources for Na-ion electrochemical works. The authors are also grateful to Prof. Richard Walton and Dr. Craig Hiley for a meaningful discussion on XRD data analysis as well as to Dr. Ivan Prokes and Dr. Michael Hope for a meaningful discussion on NMR data interpretation. We also would like to thank Dr. Marc Walker and Dr. Christopher Waldron for the technical support on XPS measurement and data analysis. We would like to acknowledge Nick Green at the Faraday Institution for invaluable support and resource management throughout the project as well as the University of St. Andrews for useful discussion during all experimental and data analysis activities. We also would like to gratefully acknowledge the AceOn Group for the technical support and scientific inputs.

■ REFERENCES

(1) Olivetti, E. A.; Ceder, G.; Gaustad, G. G.; Fu, X. Lithium-Ion Battery Supply Chain Considerations: Analysis of Potential Bottlenecks in Critical Metals. *Joule* **2017**, *1* (2), 229–243.

(2) Harper, G.; Sommerville, R.; Kendrick, E.; Driscoll, L.; Slater, P.; Stolkin, R.; Walton, A.; Christensen, P.; Heidrich, O.; Lambert, S.; et al. Recycling lithium-ion batteries from electric vehicles. *Nature* **2019**, *575* (7781), 75–86.

(3) Yang, S.; Zhang, F.; Ding, H.; He, P.; Zhou, H. Lithium Metal Extraction from Seawater. *Joule* **2018**, *2* (9), 1648–1651.

(4) Tran, M. K.; Rodrigues, M.-T. F.; Kato, K.; Babu, G.; Ajayan, P. M. Deep eutectic solvents for cathode recycling of Li-ion batteries. *Nature Energy* **2019**, *4* (4), 339–345.

(5) Hasa, I.; Mariyappan, S.; Saurel, D.; Adelhelm, P.; Koposov, A. Y.; Masquelier, C.; Croguennec, L.; Casas-Cabanas, M. Challenges of today for Na-based batteries of the future: From materials to cell metrics. *J. Power Sources* **2021**, *482*, 228872.

(6) Vaalma, C.; Buchholz, D.; Weil, M.; Passerini, S. A cost and resource analysis of sodium-ion batteries. *Nature Reviews Materials* **2018**, *3* (4), 18013.

(7) Zhang, J.; Wang, W.; Wang, W.; Wang, S.; Li, B. Comprehensive Review of P2-Type Na2/3Ni1/3Mn2/3O2, a Potential Cathode for Practical Application of Na-Ion Batteries. *ACS Appl. Mater. Interfaces* **2019**, *11* (25), 22051–22066.

(8) Cai, Z.; Wang, S.; Tao, M.; Li, Q.; Mei, H.; Ahsan, Z.; Ma, Y.; Yu, Z.; Song, G.; Yang, W.; et al. Construction of environmental-stable and high-rate layered oxide cathodes for sodium-ion batteries. *Journal of Energy Storage* **2023**, *74*, 109391.

(9) Sun, Y.; Guo, S.; Zhou, H. Adverse effects of interlayer-gliding in layered transition-metal oxides on electrochemical sodium-ion storage. *Energy Environ. Sci.* **2019**, *12* (3), 825–840.

(10) Rudola, A.; Sayers, R.; Wright, C. J.; Barker, J. Opportunities for moderate-range electric vehicles using sustainable sodium-ion batteries. *Nature Energy* **2023**, *8* (3), 215–218.

(11) Hwang, J.-Y.; Myung, S.-T.; Sun, Y.-K. Sodium-ion batteries: present and future. *Chem. Soc. Rev.* **2017**, *46* (12), 3529–3614.

(12) Desai, P.; Forero-Saboya, J.; Meunier, V.; Rousse, G.; Deschamps, M.; Abakumov, A. M.; Tarascon, J.-M.; Mariyappan, S. Mastering the synergy between Na3V2(PO4)2F3 electrode and electrolyte: A must for Na-ion cells. *Energy Storage Materials* **2023**, *57*, 102–117.

(13) Broux, T.; Fauth, F.; Hall, N.; Chatillon, Y.; Bianchini, M.; Bamine, T.; Leriche, J.-B.; Suard, E.; Carlier, D.; Reynier, Y.; et al. High Rate Performance for Carbon-Coated Na3V2(PO4)2F3 in Na-Ion Batteries. *Small Methods* **2019**, *3* (4), 1800215.

(14) Shin, K. H.; Park, S. K.; Nakhanivej, P.; Wang, Y.; Liu, P.; Bak, S.-M.; Choi, M. S.; Mitlin, D.; Park, H. S. Biomimetic composite architecture achieves ultrahigh rate capability and cycling life of sodium ion battery cathodes. *Applied Physics Reviews* **2020**, *7* (4), 041410.

(15) He, M.; Mejdoubi, A. E. L.; Chartouni, D.; Morcrette, M.; Troendle, P.; Castiglioni, R. High power NVPF/HC-based sodium-ion batteries. *J. Power Sources* **2023**, *588*, 233741.

(16) Subasinghe, L. U.; Satyanarayana Reddy, G.; Rudola, A.; Balaya, P. Analysis of Heat Generation and Impedance Characteristics of Prussian Blue Analogue Cathode-based 18650-type Sodium-ion Cells. *J. Electrochem. Soc.* **2020**, *167* (11), 110504.

(17) Xiao, Y.; Xiao, J.; Zhao, H.; Li, J.; Zhang, G.; Zhang, D.; Guo, X.; Gao, H.; Wang, Y.; Chen, J.; et al. Prussian Blue Analogues for Sodium-Ion Battery Cathodes: A Review of Mechanistic Insights, Current Challenges, and Future Pathways. *Small* **2024**, *20* (35), 2401957.

(18) Wang, W.; Gang, Y.; Hu, Z.; Yan, Z.; Li, W.; Li, Y.; Gu, Q.-F.; Wang, Z.; Chou, S.-L.; Liu, H.-K.; Dou, S.-X. Reversible structural evolution of sodium-rich rhombohedral Prussian blue for sodium-ion batteries. *Nat. Commun.* **2020**, *11* (1), 980.

(19) Xiang, X.; Zhang, K.; Chen, J. Recent Advances and Prospects of Cathode Materials for Sodium-Ion Batteries. *Adv. Mater.* **2015**, *27* (36), 5343–5364.

(20) Feng, Y.-H.; Lin, C.; Qin, H.; Wei, G.-X.; Yang, C.; Tang, Y.; Zhu, X.; Sun, S.; Chen, T.-L.; Liu, M.; et al. Cation-Anion Regulation Engineering in a Flame-Retardant Electrolyte toward Safe Na-Ion Batteries with Appealing Stability. *J. Am. Chem. Soc.* **2025**, *147* (19), 16107–16118.

(21) Liu, F.; Chen, Z.; Li, Y.; Fu, L.; Ju, J.; Ma, J.; Sun, Y. Sodium plating on hard carbon anodes in sodium-ion batteries: mechanisms, detection methods, and mitigation strategies. *Nanoscale Horizons* **2026**, *11* (1), 62–84.

(22) Mun, J.; Song, T.; Park, M.-S.; Kim, J. H. Paving the Way for Next-Generation All-Solid-State Batteries: Dry Electrode Technology. *Adv. Mater.* **2025**, *37* (36), 2506123.

(23) Marangon, V.; Bischof, K.; Regalado, A. A.; Keppeler, M.; Pogosova, M.; Wan, M.; Choi, J.; Fleischmann, S.; Diemant, T.;

Wohlfahrt-Mehrens, M.; et al. Cell design and chemistry of commercial sodium-ion battery cells. *J. Power Sources* **2025**, *634*, 236496.
(24) Bischof, K.; Marangon, V.; Kasper, M.; Aracil Regalado, A.; Wohlfahrt-Mehrens, M.; Holzle, M.; Bresser, D.; Waldmann, T. Evaluation of commercial 18650 and 26700 sodium-ion cells and comparison with well-established lithium-ion cells. *Journal of Power Sources Advances* **2024**, *27*, 100148.
(25) Rehm, M.; Fischer, M.; Gomez, M. R.; Schütte, M.; Sauer, D. U.; Jossen, A. Comparing the electrical performance of commercial sodium-ion and lithium-iron-phosphate batteries. *J. Power Sources* **2025**, *633*, 236290.
(26) Carter, R.; Waller, G. H.; Jacob, C.; Hayman, D.; West, P. J.; Love, C. T. First Look at Safety and Performance Evaluation of Commercial Sodium-Ion Batteries. *Energies* **2025**, *18*, 661.
(27) Nguyen, L. H. B.; Camacho, P. S.; Fondard, J.; Carlier, D.; Croguennec, L.; Palacin, M. R.; Ponrouch, A.; Courrèges, C.; Dedryvère, R.; Trad, K.; et al. First 18650-format Na-ion cells aging investigation: A degradation mechanism study. *J. Power Sources* **2022**, *529*, 231253.
(28) Asirvatham, M. C.; Nakhanivej, P.; Perry-French, V. A.; Altaf, E. F.; Loveridge, M. J.; Pathan, T. S.; McLaggan, J. D. Architectural Evolution and Advanced Joining Techniques in High-Energy-Density Cylindrical Li-Ion Cells. *Batteries* **2026**, *12*, 72.
(29) Chen, H.; Gulsoy, B.; Barai, A.; Nakhanivej, P.; Loveridge, M. J.; Marco, J. Experimental and numerical study of internal pressure of lithium-ion batteries under overheating. *Journal of Energy Storage* **2025**, *116*, 116066.
(30) Chen, T.; Liu, W.; Zhuo, Y.; Hu, H.; Guo, J.; Liu, Y.; Yan, J.; Liu, K. Copper surface doping to improve the structure and surface properties of manganese-rich cathode materials for sodium ion batteries. *Materials Chemistry Frontiers* **2019**, *3* (11), 2374−2379.
(31) Zhou, X.; Huang, X.; Cui, Y.; Zhu, Y.; Wang, L.; Wang, X.; Tang, S. Cu-Doped Spherical P2-Type Na0.7Fe0.23-xCuxMn0.77O2 Cathode for High-Performance Sodium-Ion Batteries. *ACS Appl. Mater. Interfaces* **2024**, *16* (28), 36354−36362.
(32) Li, J.; Chen, Y.; Chen, H.; Chen, J.; Chen, W.; Su, Y.; Ling, F. C.-C.; Ru, Q. Facile multi-step tactics to harvest copper-doped O3-type layered NaNi1/3Fe1/3Mn1/3O2 and mitigate capacity decay. *Electrochim. Acta* **2025**, *513*, 145616.
(33) Maddar, F. M.; Gonos, K.; Singh, M.; Compton, J.; Atkinson, D.; Capener, M. J.; Copley, M.; Hasa, I. Upscaling Sodium-Ion Battery Cells: From Aqueous Processing to Performance Assessment of Hard Carbon|Prussian White Pouch Cells. *Adv. Energy Mater.* **2025**, *n/a* (n/a), No. e05344.
(34) Watts, T. J.; Smart, M. C.; Manthiram, A. Differentiating the Synergistic Interactions Between Li+ Salts and Cyclic to Linear Carbonate Ratios to Enable Wide-Temperature Performance of Lithium-Ion Batteries. *Adv. Funct. Mater.* **2026**, *36* (1), No. e11694.
(35) Lee, Y.; Lee, J.; Kim, H.; Kang, K.; Choi, N.-S. Highly stable linear carbonate-containing electrolytes with fluoroethylene carbonate for high-performance cathodes in sodium-ion batteries. *J. Power Sources* **2016**, *320*, 49−58.
(36) Shipitsyn, V.; Jayakumar, R.; Zuo, W.; Yin, W.; Huber, E.; Ma, L. The impact of fluoroethylene carbonate additive on charged sodium ion electrodes/electrolyte reactivity studied using accelerating rate calorimetry. *J. Electrochem. Soc.* **2023**, *170* (11), 110501.
(37) Li, Y.; Li, Y.; He, J.; Wang, S.; Pan, H. Elucidating the Formation of Electrode-Electrolyte Interphases during Formation for Long-Life Na-Ion Batteries. *ACS Appl. Mater. Interfaces* **2025**, *17* (27), 39605−39615.
(38) Samoylova, N. Y.; Vasin, R. N.; Sumnikov, S. V.; Ponomareva, O. Y.; Donets, M. E.; Korneeva, E. A.; Andreev, E. V. Effect of drying on the polyaniline-coated Prussian white cathode material for sodium-ion batteries. *J. Phys. Chem. Solids* **2025**, *204*, 112762.
(39) Stevens, D. A.; Dahn, J. R. The Mechanisms of Lithium and Sodium Insertion in Carbon Materials. *J. Electrochem. Soc.* **2001**, *148* (8), A803.
(40) Yabuuchi, N.; Yano, M.; Yoshida, H.; Kuze, S.; Komaba, S. Synthesis and electrode performance of O3-type NaFeO2-NaNi1/2Mn1/2O2 solid solution for rechargeable sodium batteries. *J. Electrochem. Soc.* **2013**, *160* (5), A3131.
(41) Yao, H.-R.; Wang, P.-F.; Gong, Y.; Zhang, J.; Yu, X.; Gu, L.; OuYang, C.; Yin, Y.-X.; Hu, E.; Yang, X.-Q.; Stavitski, E.; Guo, Y.-G.; Wan, L.-J. Designing air-stable O3-type cathode materials by combined structure modulation for Na-ion batteries. *J. Am. Chem. Soc.* **2017**, *139* (25), 8440−8443.
(42) Deng, H.; Yang, Y.; Liu, L.; Pan, J.; Chen, P.; Shi, Z. Improving the Crystal Stability of O3-type Metal Oxide Cathode Materials by Cu Substitution for Na-Ion Batteries. *Energy Fuels* **2024**, *38* (10), 9066−9071.
(43) Xu, X.; Liu, G.; Su, C.; Zhang, Y.; Wen, L. High stability of Cu-doped O3-type NaNi1/3Fe1/3Mn1/3O2 cathode material for sodium-ion battery. *Ionics* **2024**, *30* (7), 4021−4031.
(44) Wang, P. F.; Yao, H. R.; Liu, X. Y.; Zhang, J. N.; Gu, L.; Yu, X. Q.; Yin, Y. X.; Guo, Y. G. Ti-substituted NaNi0. 5Mn0. 5-xTixO2 cathodes with reversible O3- P3 phase transition for high-performance sodium-ion batteries. *Adv. Mater.* **2017**, *29* (19), 1700210.
(45) Dallaev, R.; Pisarenko, T.; Sobola, D.; Orudzhev, F.; Ramazanov, S.; Trčka, T. Brief Review of PVDF Properties and Applications Potential. *Polymers (Basel)* **2022**, *14* (22), 4793.
(46) Qahtan, T. F.; Alade, I. O.; AlArjani, A.; Rahaman, M. S. Advancements in sodium-ion batteries: An in-depth scientometric review. *Journal of Energy Storage* **2025**, *131*, 117490.
(47) Yao, A.; Benson, S. M.; Chueh, W. C. Critically assessing sodium-ion technology roadmaps and scenarios for techno-economic competitiveness against lithium-ion batteries. *Nature Energy* **2025**, *10* (3), 404−416.

NOTE ADDED AFTER ASAP PUBLICATION

Figure 6 was replaced after this paper was published ASAP on April 24, 2026. The revised version was reposted on April 28, 2026.

https://doi.org/10.1021/acsaem.5c03924
ACS Appl. Energy Mater. 2026, 9, 5555−5563